Supplementary Information (SI): Concept, absolute calibration and validation of a new, benchtop laser imaging polar nephelometer

Supplementary Section S1:

Supplementary tables:

Table S1. size specification of the PSL samples. A material density of 1050 kg m^{-3} for PSL was used for diameter conversion.

Certified geometric mean diameter (nm)	Specified coefficient of variation	AAC Aerodynamic diameter set point (nm)	Equivalent volume diameter of AAC aerodynamic diameter set point (nm)
600 ± 9	0.07	620	603
240 ± 5	0.05	250	242

Table S2. AAC aerodynamic diameter set point and corresponding equivalent volume diameter for tested DEHS aerosols. A material density of 900 kg m^{-3} for DEHS was used for diameter conversion.

AAC aerodynamic diameter set point (nm)	Equivalent volume diameter of sample, d_{ev} (nm)
200	215
250	267
400	425
600	636
800	847

Table S3. Parameters of the experiments performed with AAC selected mono-disperse DEHS aerosol samples: AAC set point (aerodynamic diameter), corresponding volume equivalent diameter (d_{ev}; converted using material density of 900 kg m^{-3} and assuming spherical shape), particle number concentration measured by the CPC (N_{cpc}). The following columns present size distribution parameters retrieved from phase functions measured by the uNeph using the least square minimization scheme: geometric mean diameter (d_{ret}), geometric standard deviation (GSD_{ret}), and particle number concentration (N_{ret}). The last two columns present the relative deviation of retrieved parameters from corresponding independently determined values.

AAC set point	AAC d_{ev}	N_{CPC} mean±SD	d_{ret}	GSD_{ret}	N_{ret}	$(d_{ev} - d_{ret}) / d_{ev}$	$(N_{CPC} - N_{ret}) / N_{CPC}$
(nm)	(nm)	(cm^{-3})	(nm)	(-)	(cm^{-3})	(%)	(%)
200	215	189.5 ± 8	214	1.035	185.7	-0.5%	+2.0%
400	425	494.3 ± 11	413	1.065	514	-2.8%	-4.0%
600	636	58.8 ± 4	612	1.05	61.8	-3.8%	-5.0%
800	847	70.2 + 5	817	1.06	73.7	-3.5%	-6.0%

Supplementary figures:

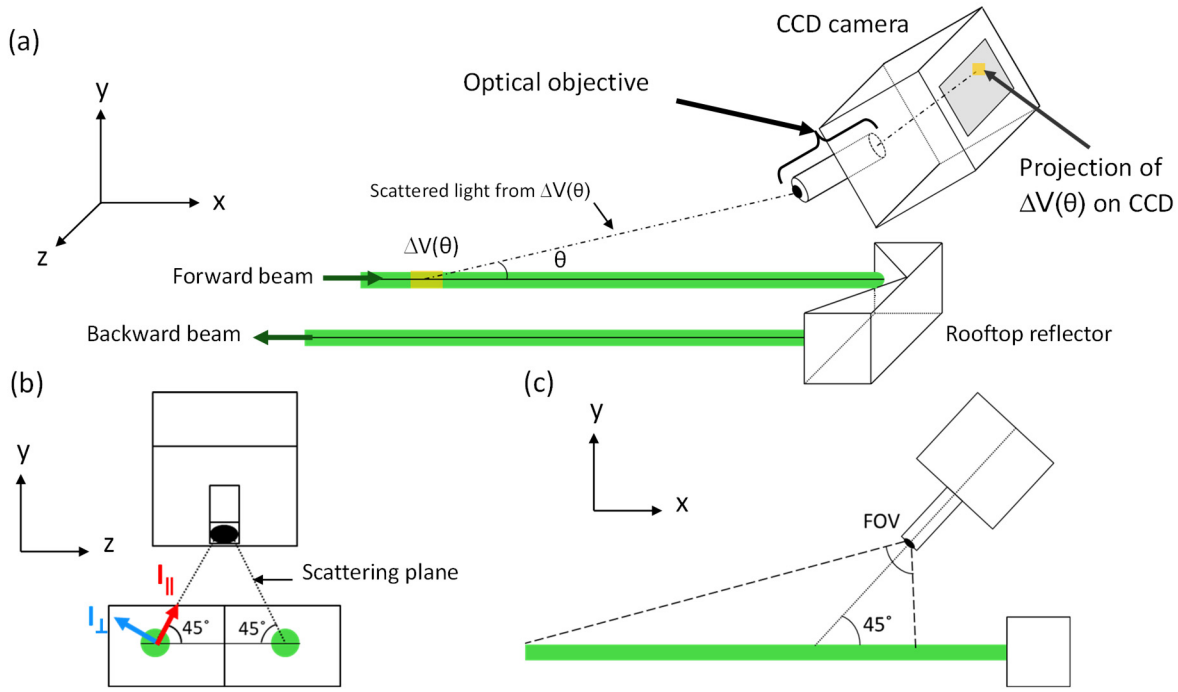

Figure S1. Scattering geometry in the uNeph

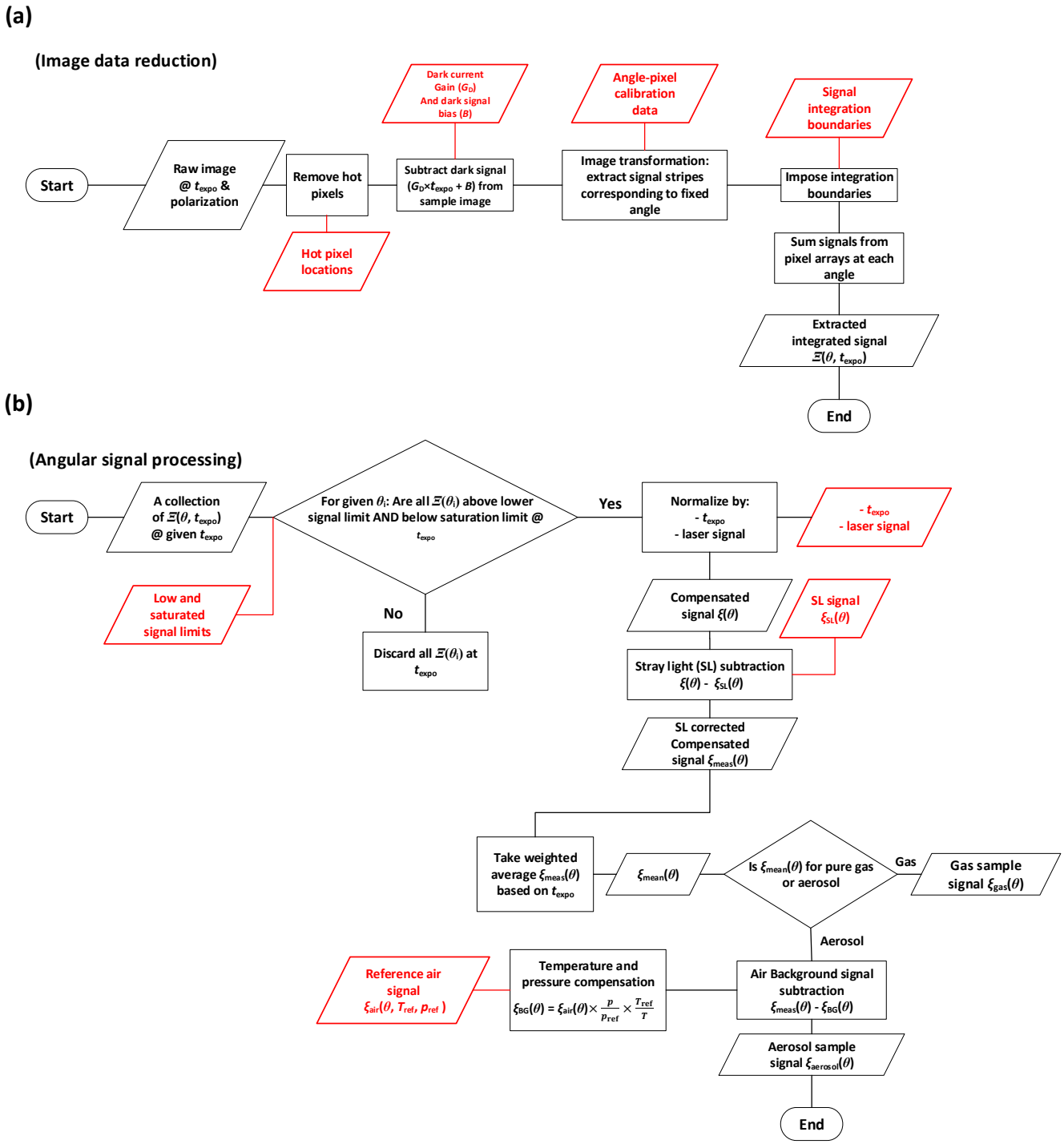

Figure S2. Flowchart of all the data processing steps. Calibration and external auxiliary data are shown as red boxes and text. Methods and inputs with red lines are the external data used in the data processing.

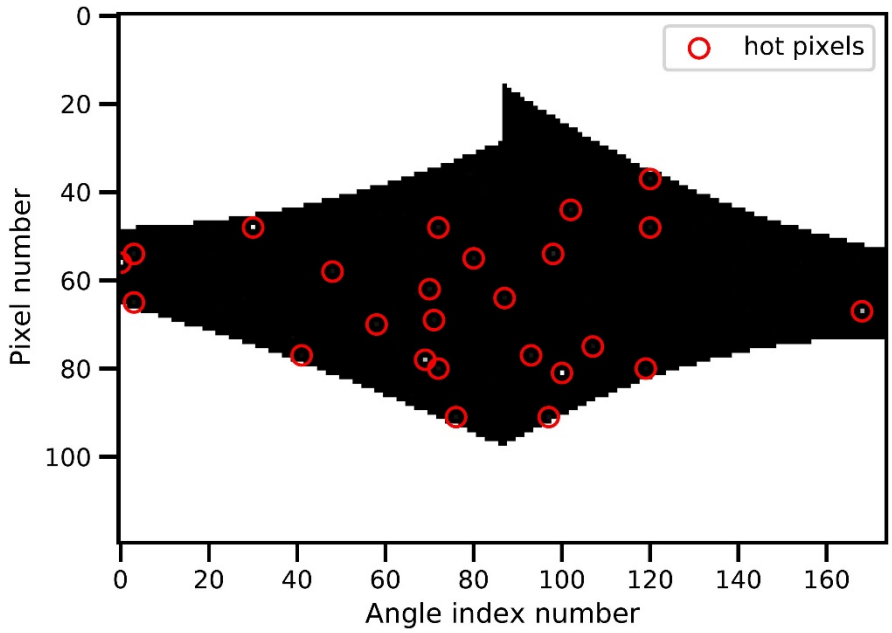

Figure S3. Dark image in angle-pixel coordinate with hot pixels specified. To better visualize the hot pixels, the dark image shown corresponds to a dark image obtained with exposure time of 900 s.

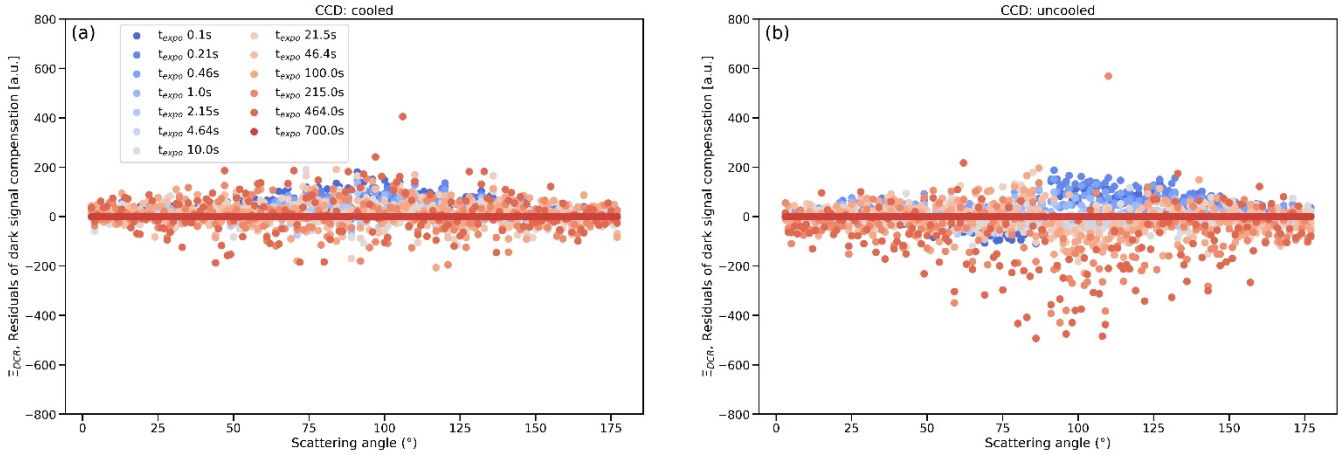

Figure S4. Residual signal from dark signal correction on the data for the cooled (Panel a) and uncooled CCD (Panel b). The constants $G_{DS}(\theta)$ and $\Xi_{PB}(\theta)$ were not perfectly optimized for the backward angle range (90°-180°) in the uncooled case leaving some systematic exposure time dependence in the residuals. Nevertheless, the residuals of ~200 a.u. or less for exposure times shorter than 215 s are sufficiently small given that the upper limit of valid signals (saturation) occurs at around $2 \cdot 10^5$ to $2 \cdot 10^6$ a.u. (Fig. S12).

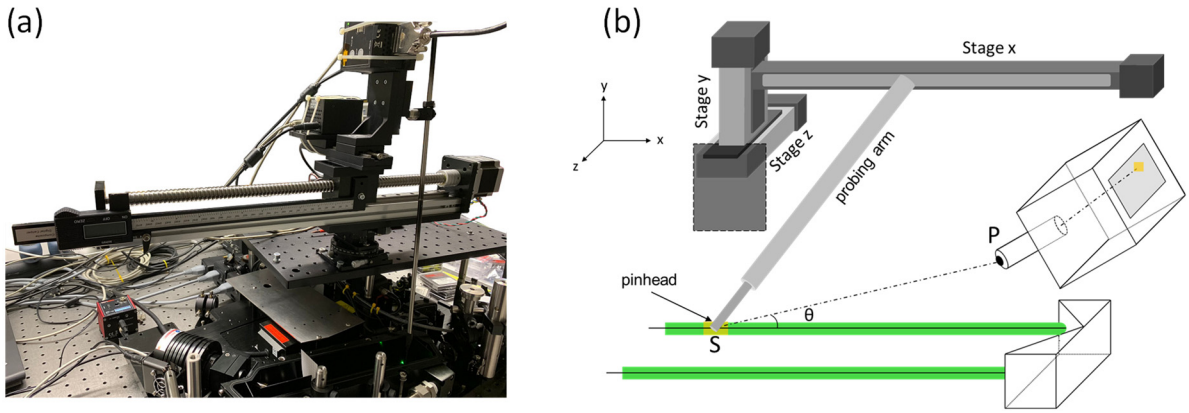

Figure S5. (a) A picture of the 3D positional probe mounted on top the uNeph. (b) a 3D scheme of the positional probe, probing an example point S along the laser beam of the uNeph.

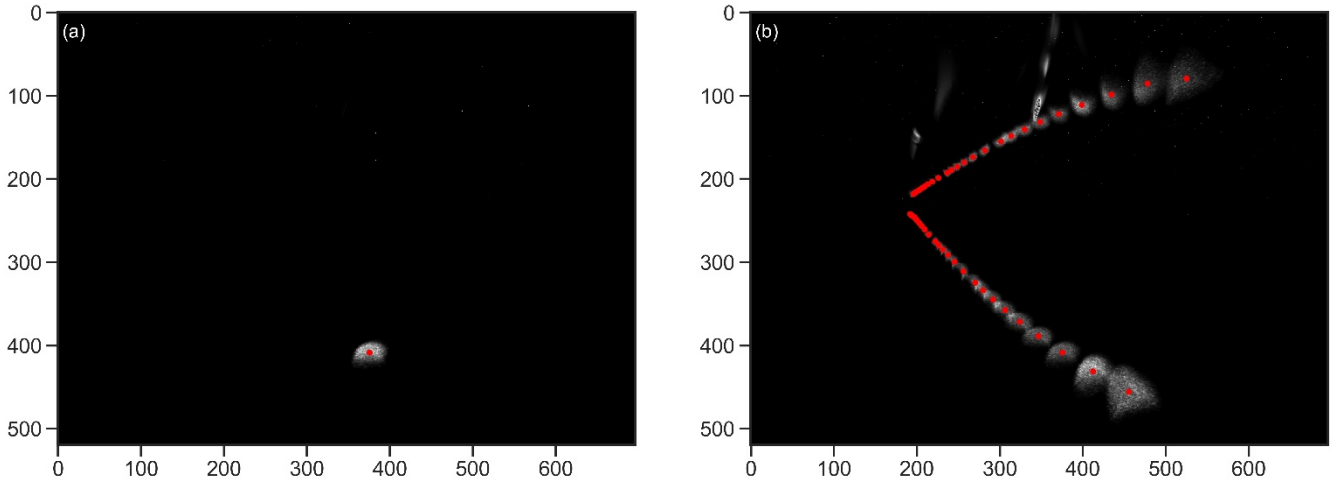

Figure S6. (a) An example of angular calibration image data at a point corresponding to the scattering angle of approximately 68˚. (b) a composite image of all calibration data. The red dots in the images corresponds to the pixel of the centre of mass of the given spots with is considered as the pixel corresponding to the location of the 3D positional probe's pinhead. It should be noted that the spots closer to the detection units appear larger while the spots further from the detection unit appear smaller.

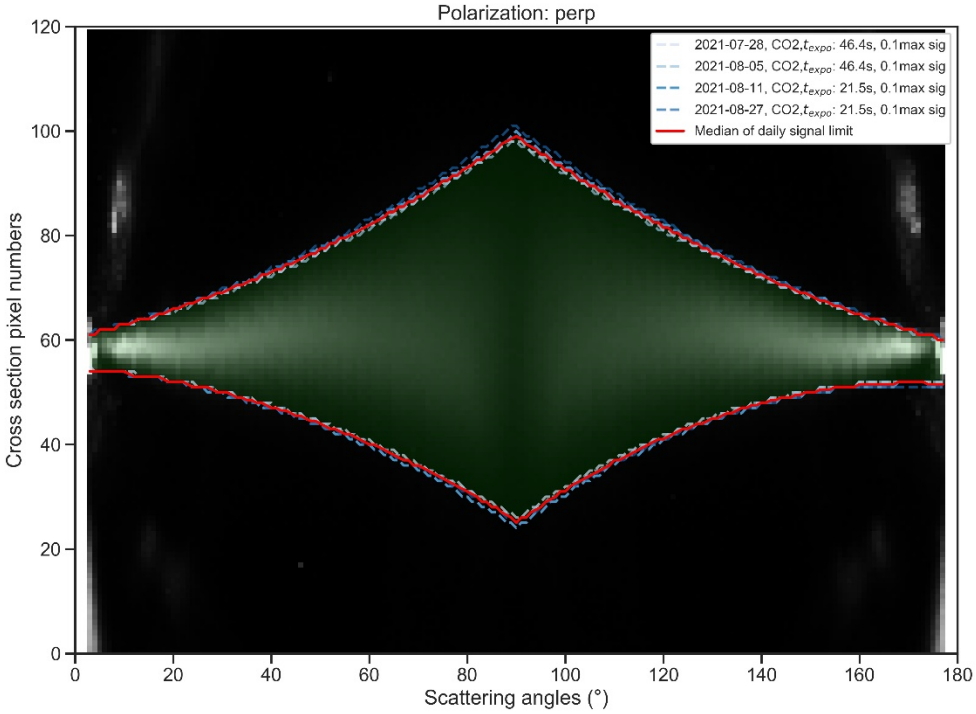

Figure S7. The signal integration limits over scattering angles obteianed from the CO_2 measurements collected in different days.

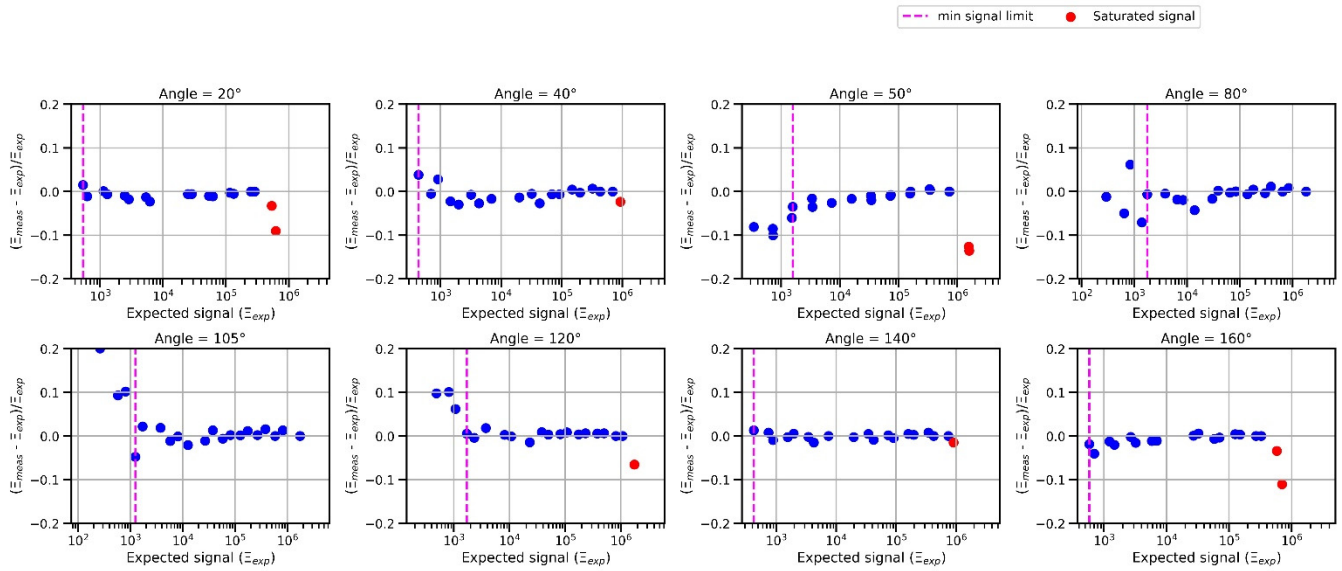

Figure S8. Relative error vs Ξ_{exp} for particle free air sample signals over different scattering angles for both polarization states and for a cooled CCD condition.

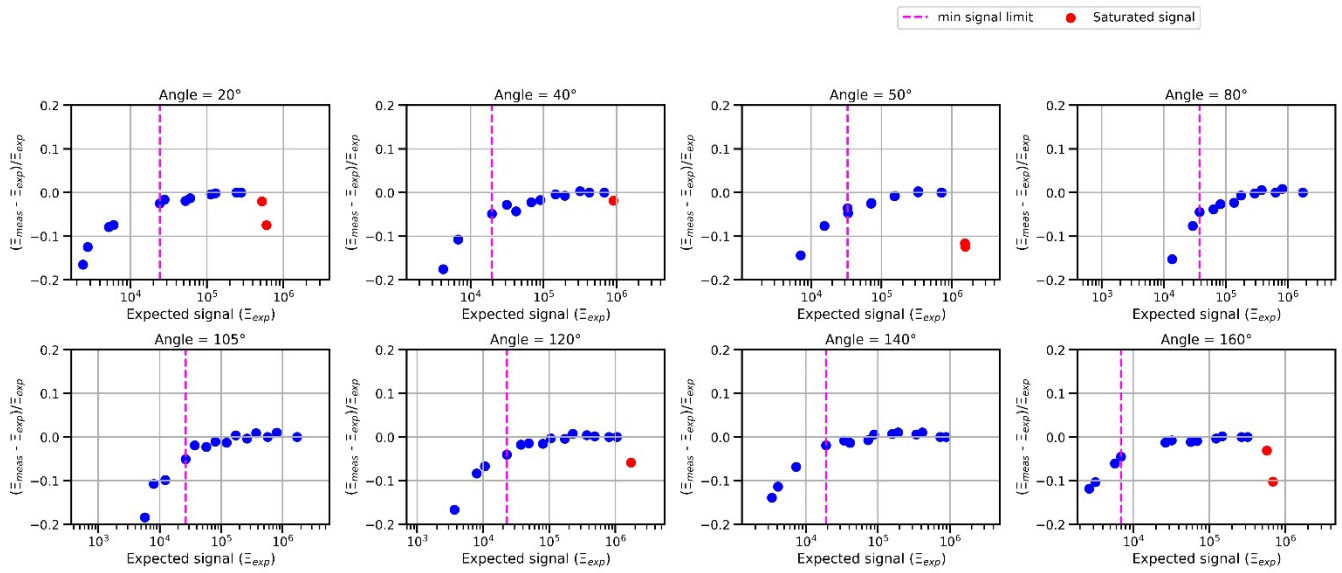

Figure S9. Relative error vs Ξ_{exp} for particle free air sample signals over different scattering angles for both polarization states and for an uncooled CCD condition.

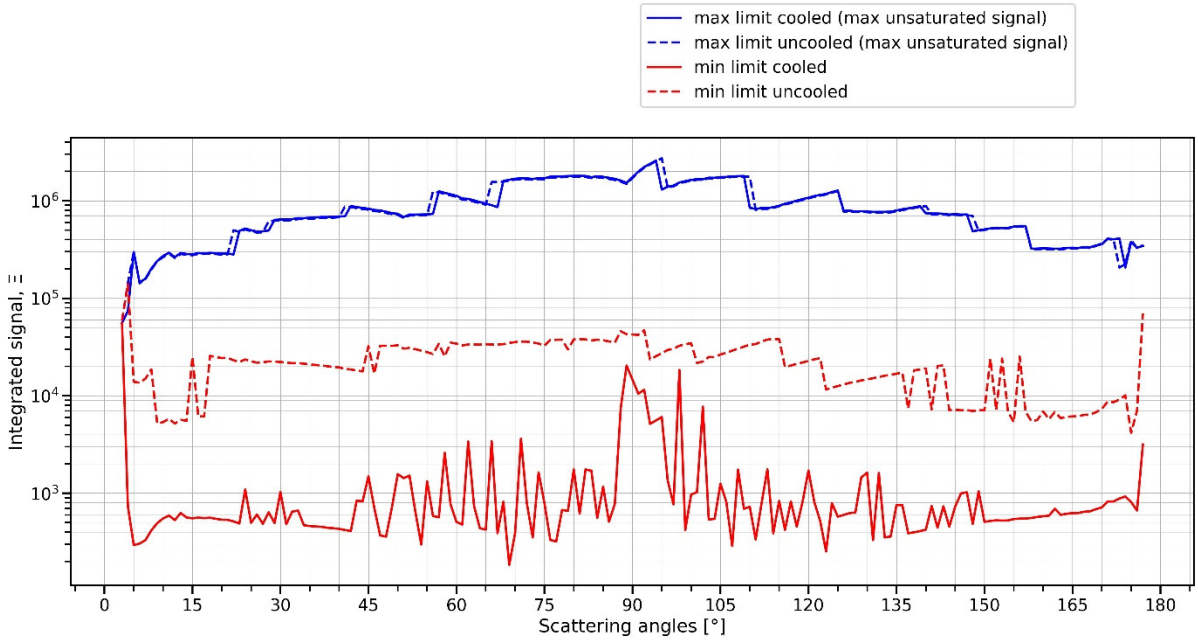

Figure S10. Lower and upper limits for valid signal for cooled (solid line) and uncooled (dashed lines) CCD cases based on air measurements taken over a broad range of t_{expo}. The upper limit is the signal above which at least one saturated pixel exists and the lower limit is the lowest signal below which the relative difference between Ξ_{exp} and Ξ_{meas} increases above 6%.

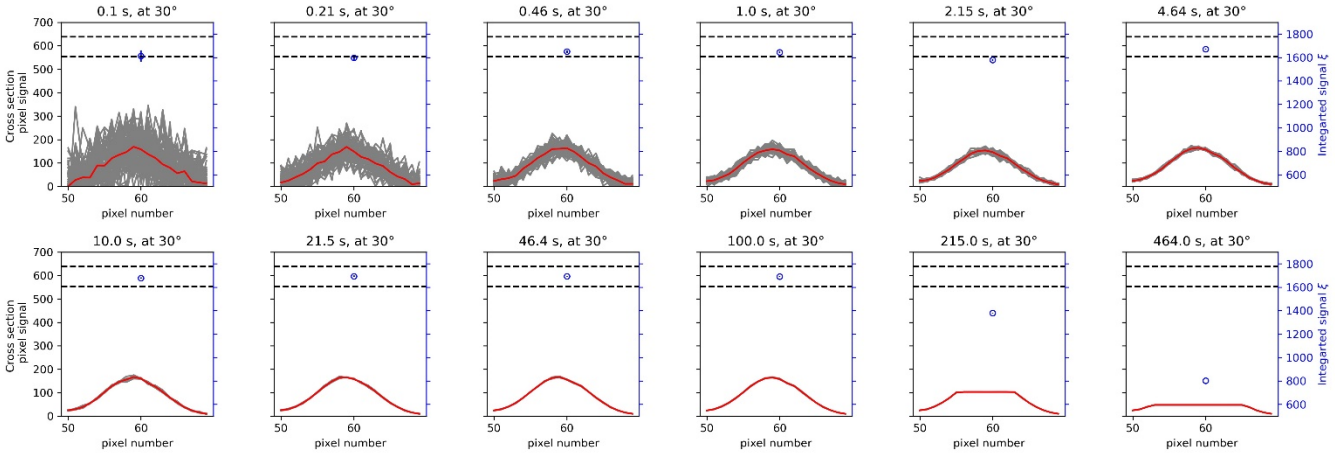

Figure S11. Cross section signal (normalized by t_{expo} and laser power signal) and integrated signal (normalized by t_{expo} and laser power signal) behaviour over a range of exposure times (see plot titles) for filtered air samples at a scattering angle of 30°. Samples taken at polarization state 2. The mean integrated signal, ξ, with corresponding standard error of the mean as error bars in blue, plotted against right ordinate scale. The horizontal dashed line indicates ±5% variation around the mean ξ at t_{expo} = 100 s.

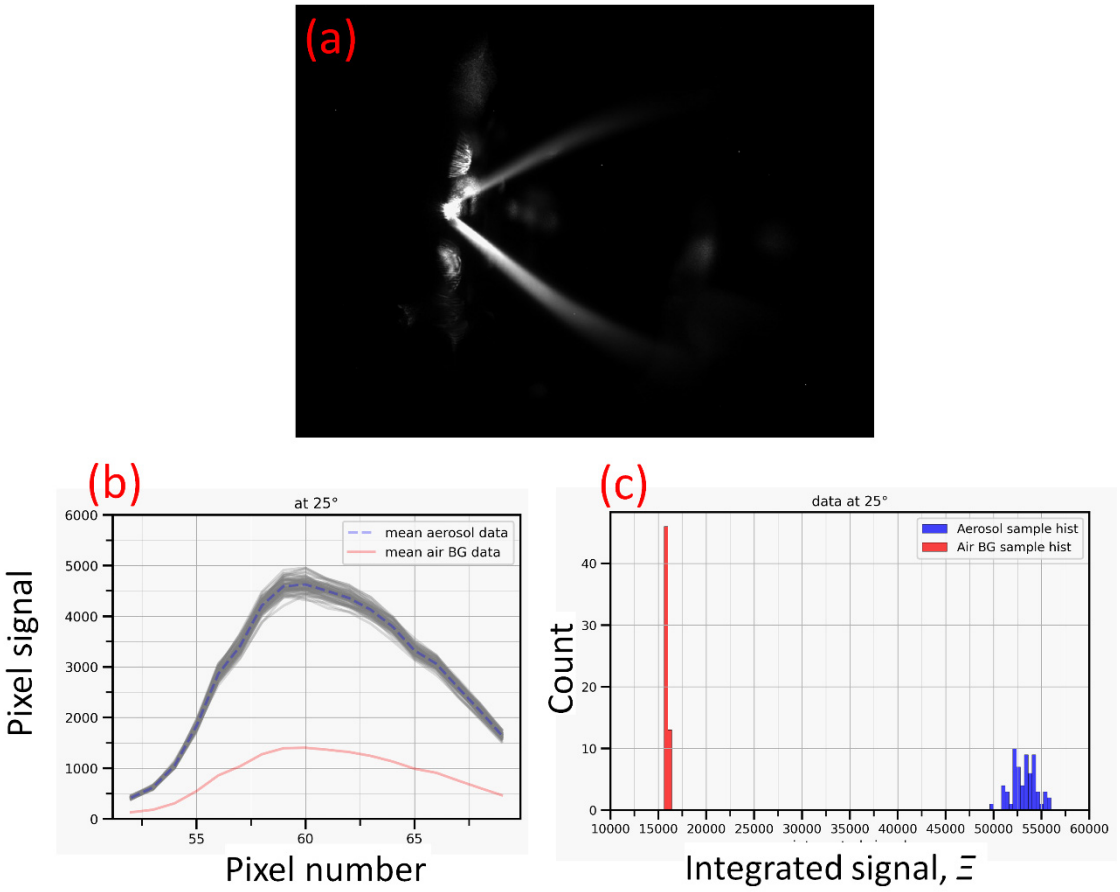

Figure S12. Results for 200 nm DEHS aerosol test case with t_{expo} = 4.64 s, particle number concentration: 1000 #/cc. (a) is an example of a single frame of raw data captured by uNeph for this aerosol sample, (b) are the signals in cross-sectional pixel at scattering angle of 25˚. The grey lines are the aerosol samples in each sample frame (64 sample frames), the blue line is the mean of aerosol signals, and the red line is the mean of background (BG) air (60 sample frames, with t_{expo} = 4.64 s). (c) is the histogram of the integrated signal Ξ_{air} (red) and $\Xi_{aerosol}$ (blue) over the sampled frames.

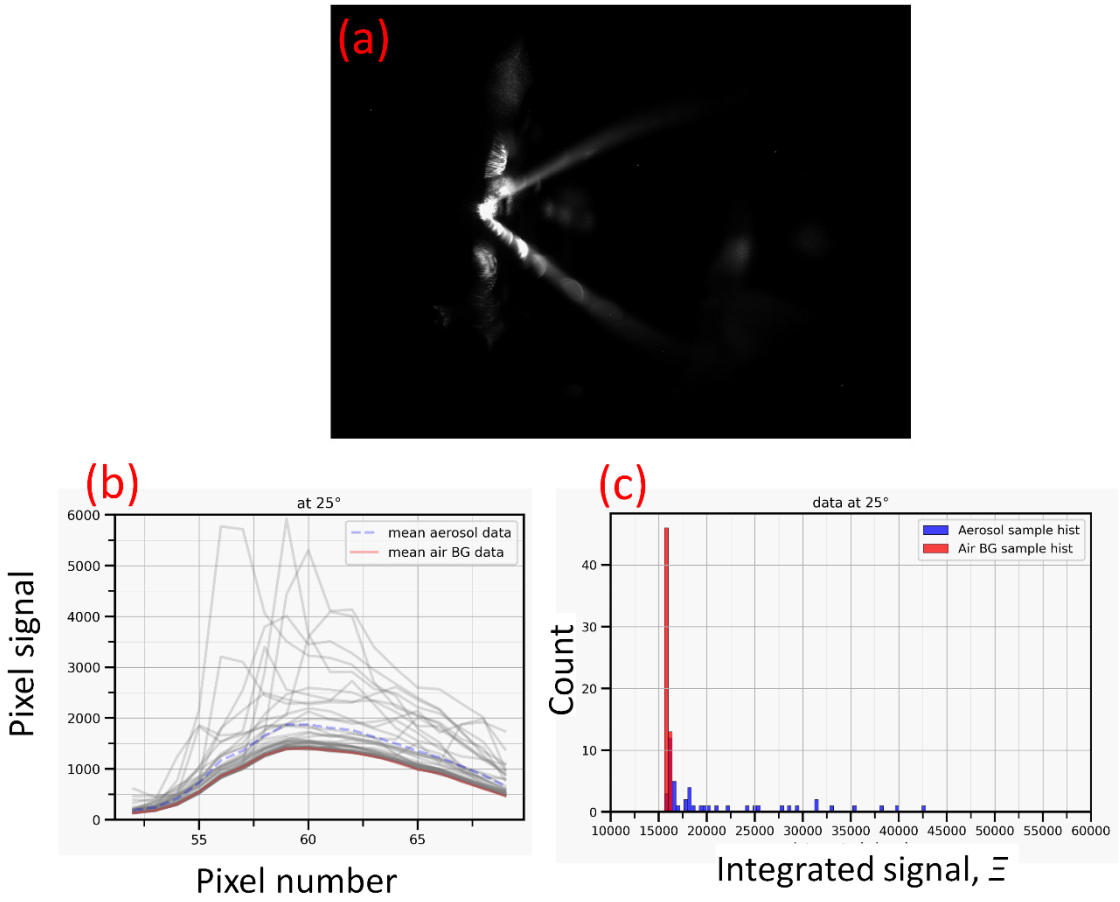

Figure S13. 200 nm DEHS test case with t_{expo} = 4.64 s and concentration: 1 #/cc (47 sample frames). The panels (a) to (c) are to the same as in Fig. S12.

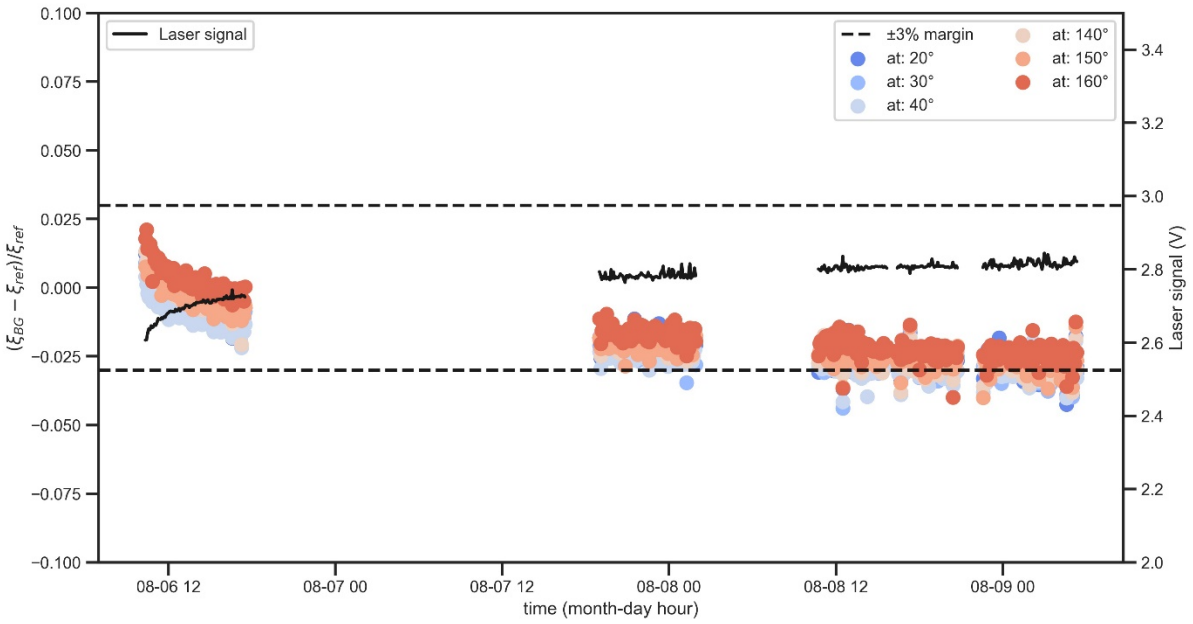

90

Figure S14. Relative difference of air background (ξ_{BG}) to an arbitrary air reference point (ξ_{ref}, sample taken on the 2021-08-10 17:43 - 17:47) during a multiday measurement. This is shown for measurements of polarization state 1 at different scattering angles (5 min averages). The horizontal dashed lines indicate ±3% around the arbitrarily chosen reference point ξ_{ref}.

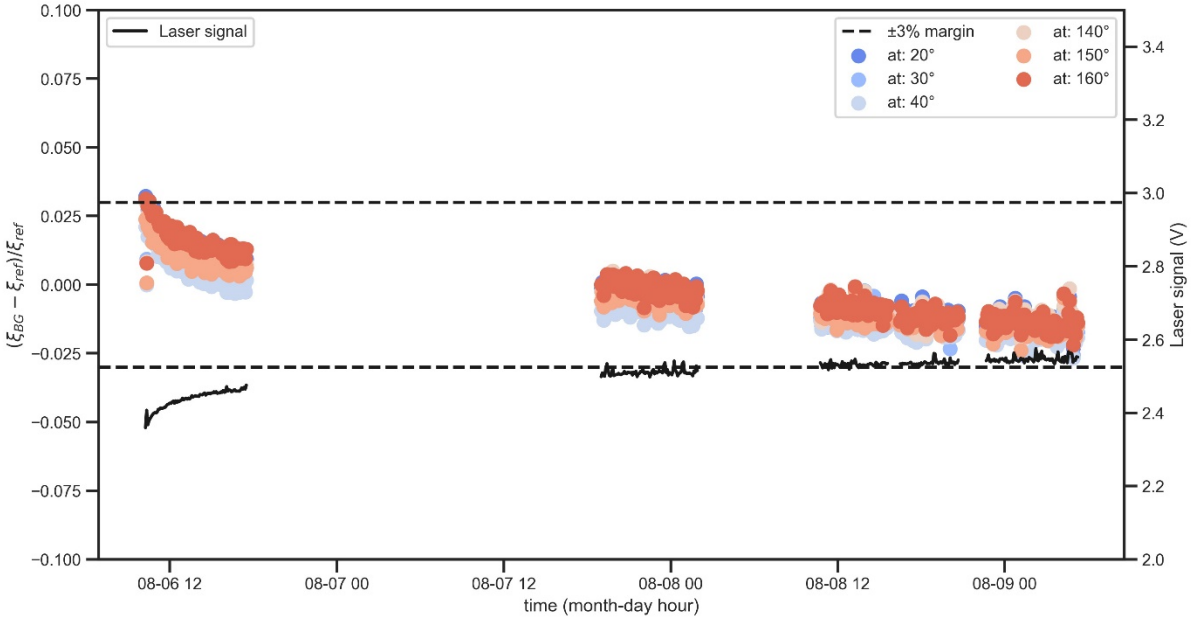

95

Figure S15. Same as Fig. S14 for presenting polarization state 2 results with the arbitrary air reference point taken on the 2021-08-10 18:21 - 18:26).

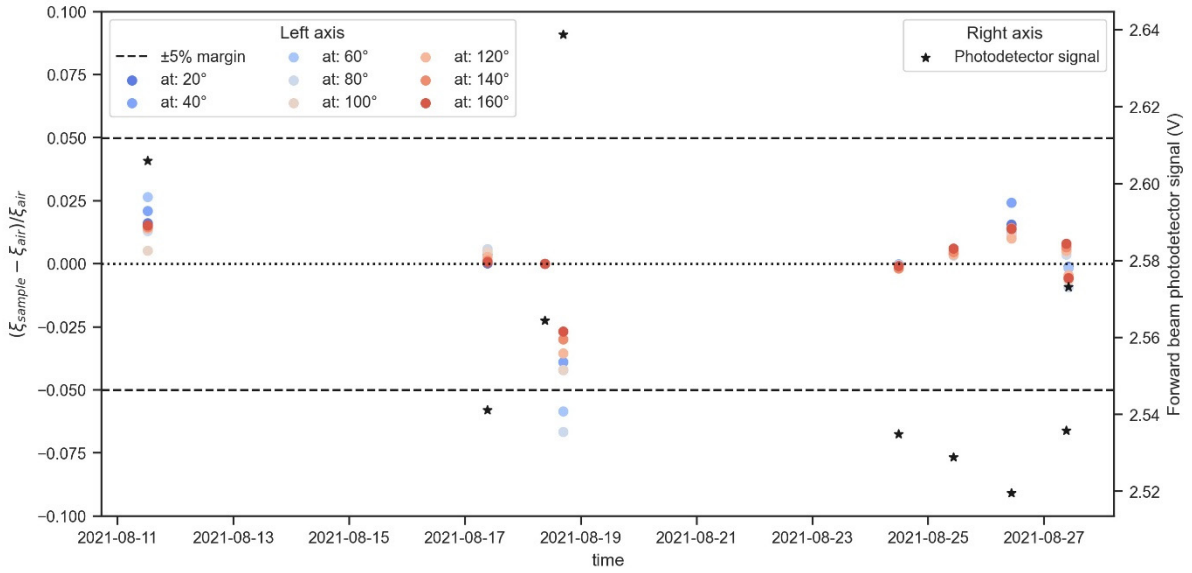

Figure S16. Day to day particle-free air signal variability. The reference air signal assumed to calculate the relative difference was the sample taken on 2021-08-18.

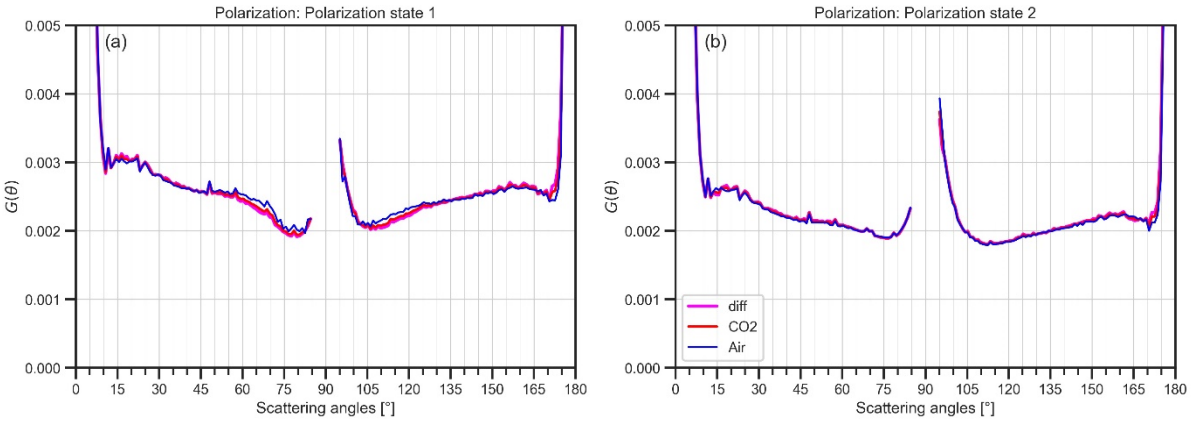

Figure S17. (a) and (b) respectively shows $G_1(\theta)$ and $G_2(\theta)$ values derived from difference in CO_2 and air measurements (diff) and from individual gas (CO_2 and air) measurements.

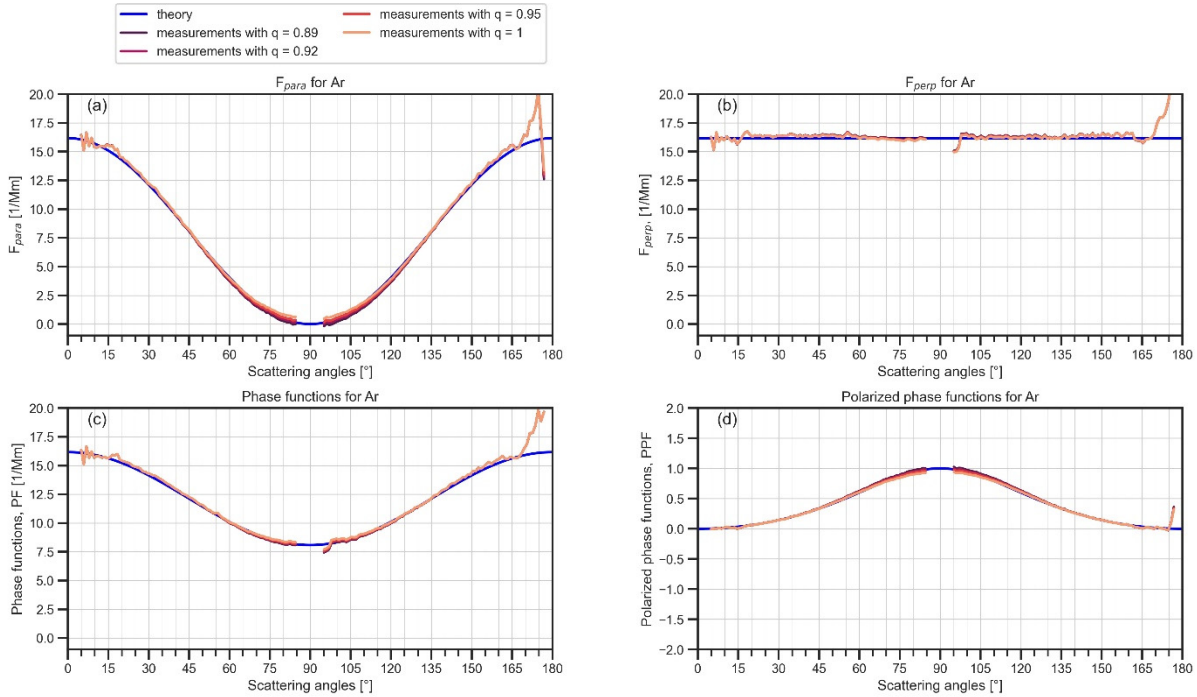

Figure S18. (a) parallel phase function, F_{para}, (b) perpenicular phase function, F_{perp}, (c) phase function F_{11}, and (d) polarized phase function, $-F_{11}/F_{12}$, for uNeph measurements of Ar gas, given different q value assumptions. The blue line corresponds to the theoretical angular light scattering of Ar based on Rayleigh scattering.

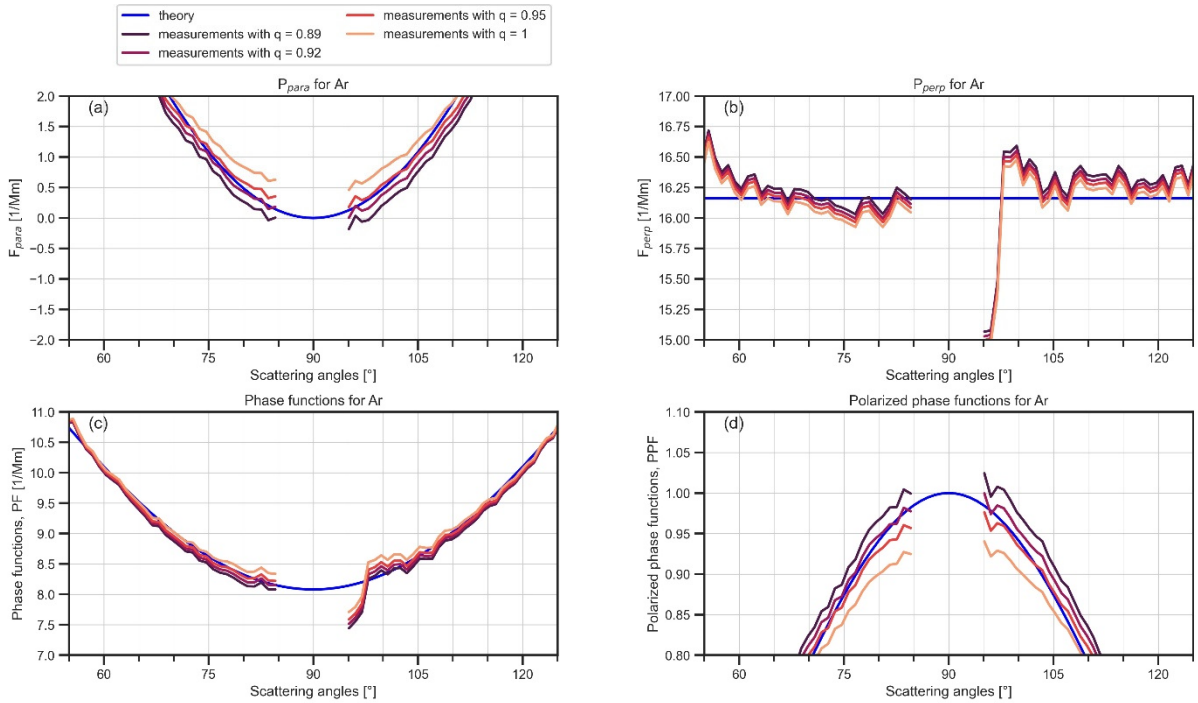

Figure S19. Same as Fig. S18 but for zooming in to angle range from 55° to 125°. We selected $|q_i| = 0.92$ and $|q_i| = 0.95$ as appropriate values for forward and backward beams, respectively.

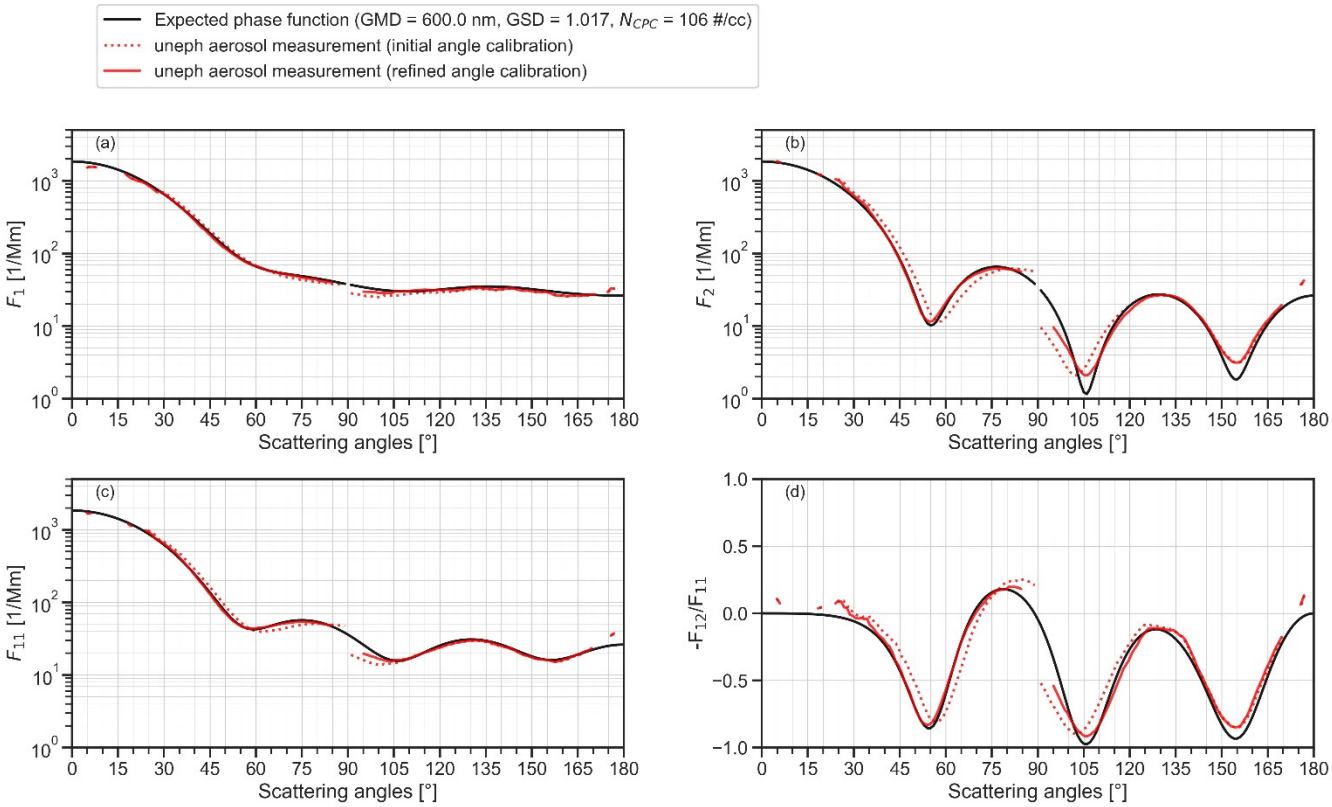

Figure S20. Expected and measured results for a PSL size standard with geometric mean diameter (*GMD*)=600 nm for (a) F_1, (b) F_2, (c) F_{11} and (d) $-F_{12}/F_{11}$. The expected curves are based on Mie theory for homogeneous spheres constrained with certified mean particle diameter (600 nm), geometric standard deviation (*GSD* = 1.017) inferred from reported coefficient of variation and particles number concentration measured by a CPC (N_{CPC}). The uNeph measurement is processed with finally calibrated *q*-values and two different angle calibration curves: the red dashed line represents initial angle calibration, whereas the red solid line represents refined angle calibration based on optimized pinhole center coordinates.

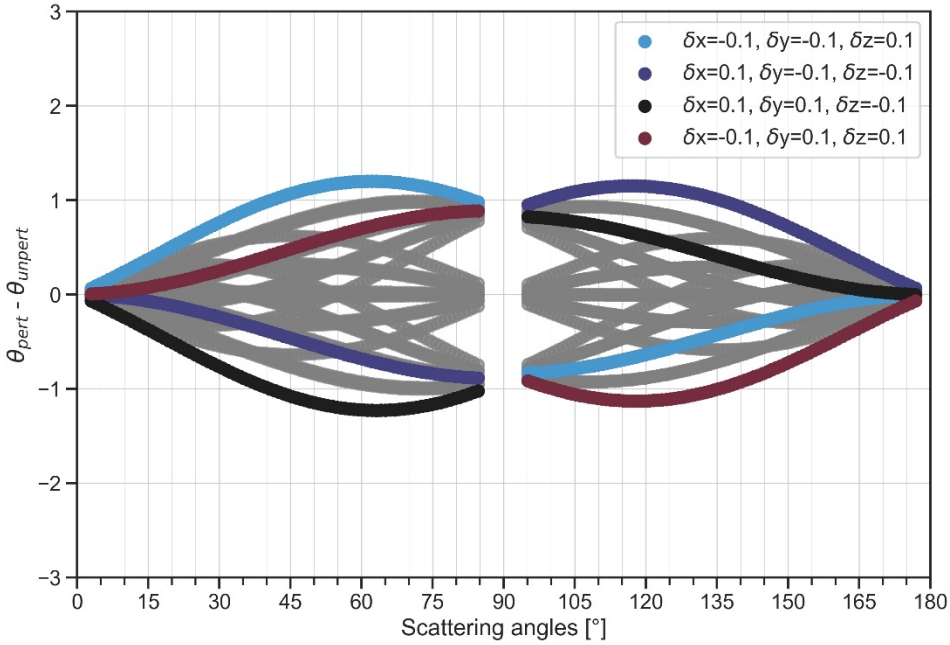

Figure S21. Angle difference between perturbed and unperturbed case. The unperturbed case is based on the best pinhole estimate.

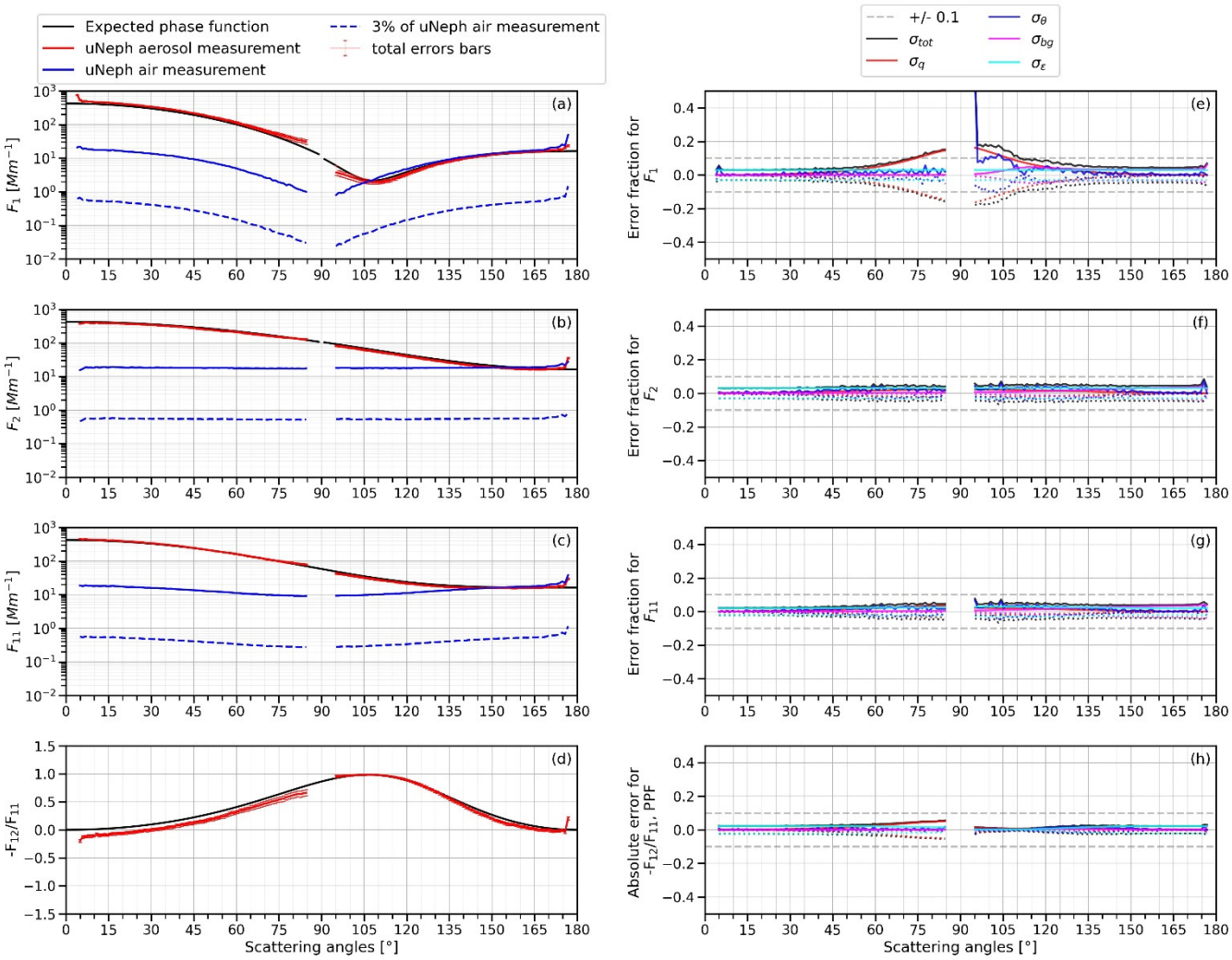

Figure S22. (a, b, c, d) angular light scattering measurements with total errors for 250 nm (AAC aerodynamic set point) DEHS aerosol particles at high concentration (3010 #/cc). (e, f, g,) relative contributions of considered error factors for F_1, F_2, and F_{11}. (h) Absolute contributions of considered error factors for $-F_{12}/F_{11}$

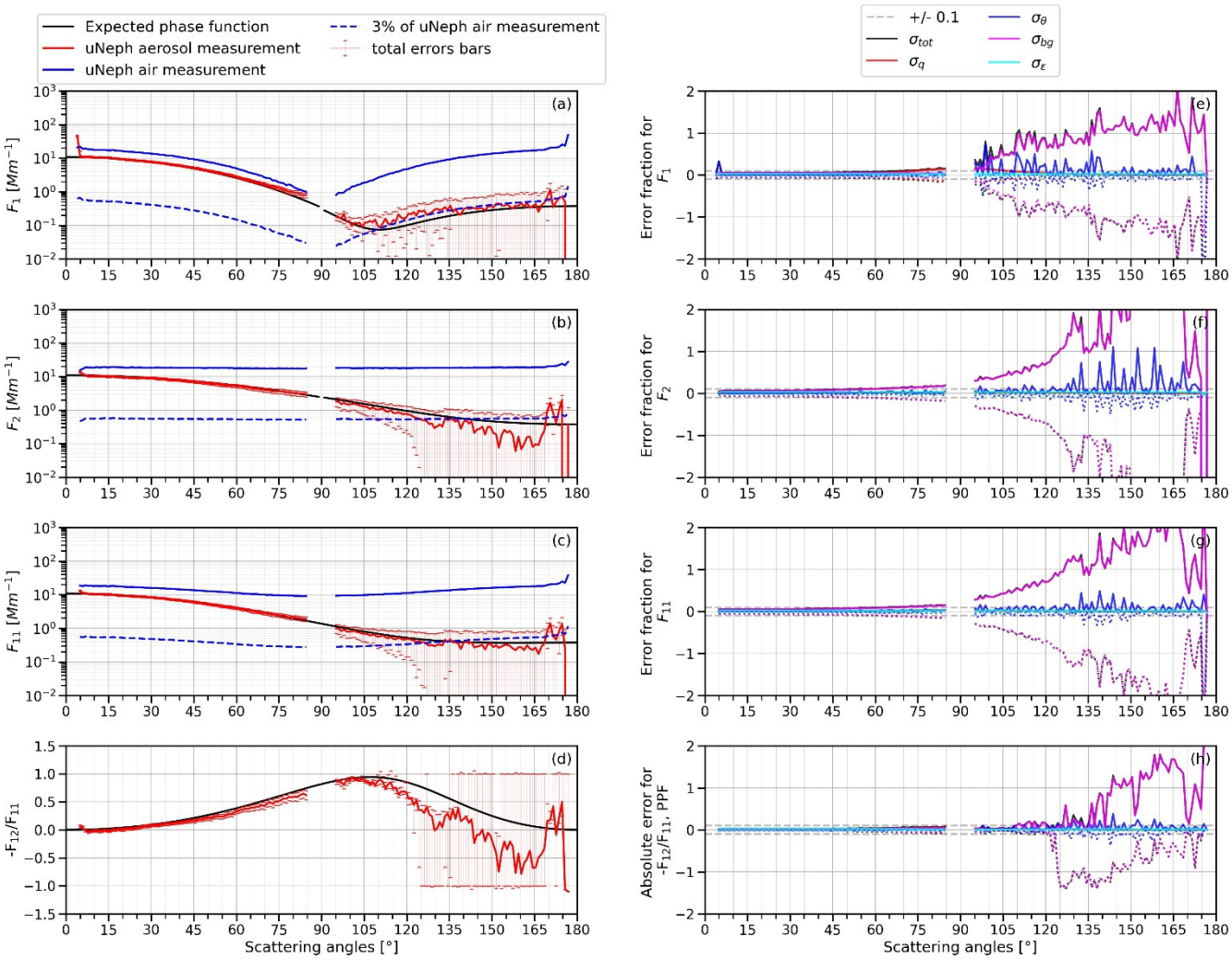

Figure S23. (a, b, c, d) angular light scattering measurements with total errors for 250 nm (AAC aerodynamic set point) DEHS aerosol particles at low concentration (70 #/cc). (e, f, g,) relative contributions of considered error factors for F_1, F_2, and F_{11}. (h) Absolute contributions of considered error factors for -F_{12}/ F_{11}.

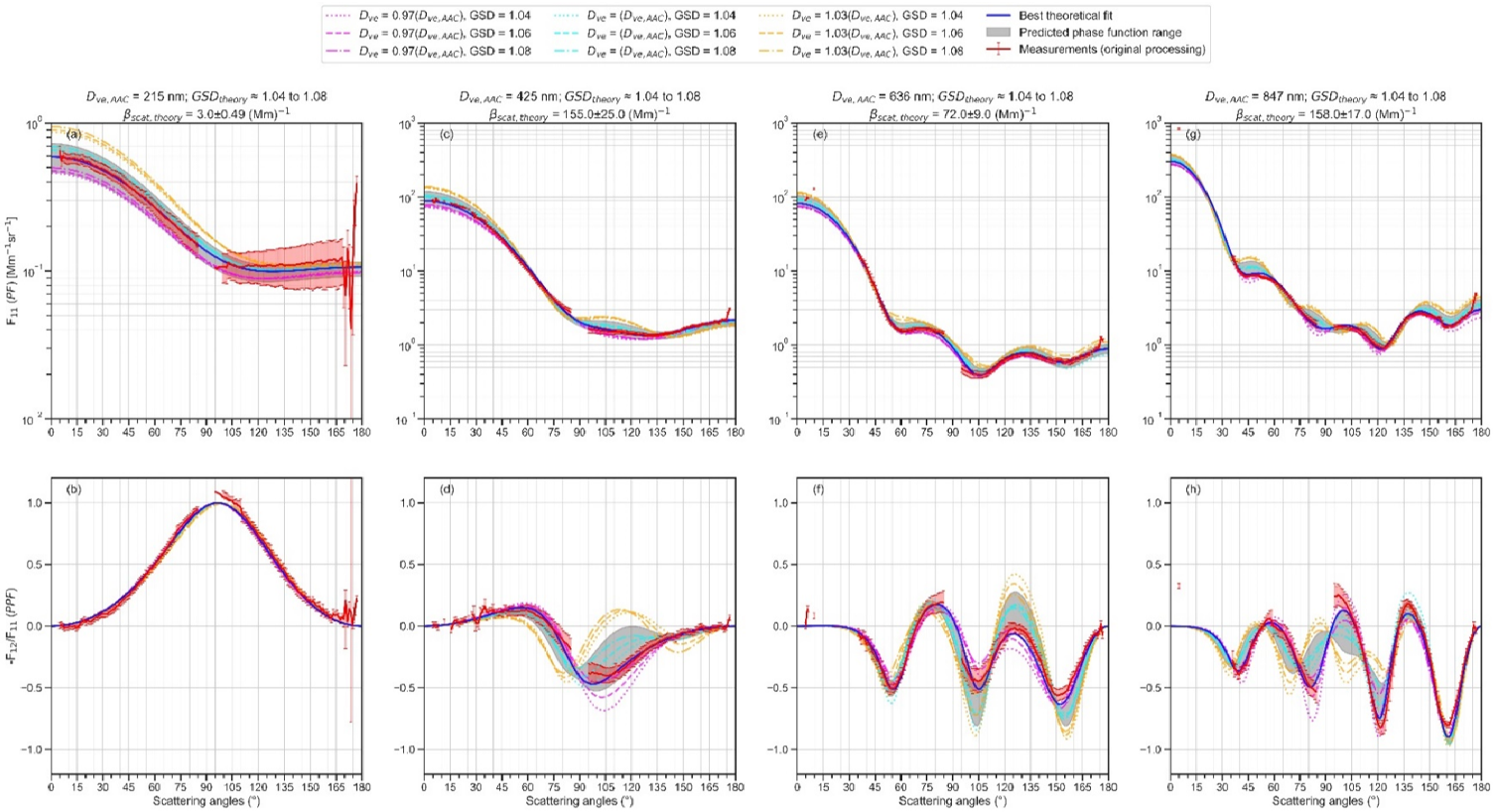

Figure S24. Same as Figure 6 but for additional Mie curves for each test cases. The additional Mie curve were simulated at three different dm corresponding to the AAC set point, DVE, AAC (cyan lines), and 0.97DVE, AAC (magenta lines) and 1.03DVE, AAC (yellow lines) which are respectively the high and low extremes of DVE, AAC within the assumed ¬error range of 3%. Mie curve at each median size case were simulated for three different GSD cases of 1.04, 1.06 and 1.08 (demonstrated at different line styles) and cover the extremes and mid values within the expected variation range of the GSD.